

Cite this: *Phys. Chem. Chem. Phys.*, 2011, **13**, 9469–9482

www.rsc.org/pccp

PAPER

# On the formation of ozone in oxygen-rich solar system ices *via* ionizing radiation

Courtney P. Ennis,<sup>a</sup> Chris J. Bennett<sup>ab</sup> and Ralf I. Kaiser<sup>\*a</sup>

Received 19th February 2011, Accepted 17th March 2011

DOI: 10.1039/c1cp20434c

The irradiation of pure molecular oxygen (O<sub>2</sub>) and carbon dioxide (CO<sub>2</sub>) ices with 5 keV H<sup>+</sup> and He<sup>+</sup> ions was investigated experimentally to simulate the chemical processing of oxygen rich planetary and interstellar surfaces by exposure to galactic cosmic ray (GCR), solar wind, and magnetospheric particles. Deposited at 12 K under ultra-high vacuum conditions (UHV), the irradiated condensates were monitored on-line and *in situ* in the solid-state by Fourier transform infrared spectroscopy (FTIR), revealing the formation of ozone (O<sub>3</sub>) in irradiated oxygen ice; and ozone, carbon monoxide (CO), and cyclic carbon trioxide (*c*-CO<sub>3</sub>) in irradiated carbon dioxide. In addition to these irradiation products, evolution of gas-phase molecular hydrogen (H<sub>2</sub>), atomic helium (He) and molecular oxygen (O<sub>2</sub>) were identified in the subliming oxygen and carbon dioxide condensates by quadrupole mass spectrometry (QMS). Temporal abundances of the oxygen and carbon dioxide precursors and the observed molecular products were compiled over the irradiation period to develop reaction schemes unfolding in the ices. These reactions were observed to be dependent on the generation of atomic oxygen (O) by the homolytic dissociation of molecular oxygen induced by electronic, S<sub>e</sub>, and nuclear, S<sub>n</sub>, interaction with the impinging ions. In addition, the destruction of the ozone and carbon trioxide products back to the molecular oxygen and carbon dioxide precursors was promoted over an extended period of ion bombardment. Finally, destruction and formation yields were calculated and compared between irradiation sources (including 5 keV electrons) which showed a surprising correlation between the molecular yields ( $\sim 10^{-3}$ – $10^{-4}$  molecules eV<sup>-1</sup>) created by H<sup>+</sup> and He<sup>+</sup> impacts. However, energy transfer by isoenergetic, fast electrons typically generated ten times more product molecules per electron volt ( $\sim 10^{-2}$ – $10^{-3}$  molecules eV<sup>-1</sup>) than exposure to the ions. Implications of these findings to Solar System chemistry are also discussed.

## Introduction

Oxygen-bearing ices are abundant on a variety of Solar System and interstellar surfaces. In the outer Solar System, solid carbon dioxide (CO<sub>2</sub>) has been detected on Galilean satellites Europa, Callisto, and Ganymede<sup>1,2</sup> and on the Saturnian moons Enceladus, Dione, Hyperion, Iapetus, and Phoebe.<sup>3,4</sup> In addition, the encounter with comet Hale-Bopp<sup>5</sup> identified a significant amount of carbon dioxide out-gassing from its nuclei ( $1.3 \times 10^{28}$  molecules s<sup>-1</sup>).<sup>6</sup> Reaching beyond the confines of the Solar System, carbon dioxide has also been identified as an abundant constituent of interstellar grains at fractions of 8–35% relative to the dominant water species.<sup>7</sup> Carbon dioxide absorptions are detected remotely by spaceborne spectroscopic facilities, such as the Infrared Space Observatory. These instruments collect light originally emitted

from field stars located behind the medium (*e.g.* Elias 16 for TMC-1) that pass through molecular cloud regions.<sup>8</sup>

On the other hand, planetary and interstellar ices bearing molecular oxygen (O<sub>2</sub>) are more difficult to detect. The elusiveness of oxygen stems from its low concentrations in icy compositions and that the molecule displays weak absorption in the infrared spectroscopic region, which is primarily used to probe the chemical make-up of distant objects.<sup>9</sup> However, condensed-phase molecular oxygen was discovered on the Jovian moons Ganymede<sup>10</sup> and Callisto<sup>11</sup> harbored within their water ice surfaces. Thought to be produced from the radiolytic destruction of the water ice,<sup>11–14</sup> oxygen molecules accumulate in aggregates that can be identified by absorption bands in the visible range of the electromagnetic spectrum. Otherwise, the existence of molecular oxygen on outer Solar System bodies can be inferred by the identification of ‘tracer’ species such as ozone (O<sub>3</sub>).<sup>15</sup> Ozone is a by-product of energetic irradiation of molecular oxygen in icy environments and is easier to detect spectroscopically, particularly if the ozone concentration has increased sufficiently over geological

<sup>a</sup> Department of Chemistry, University of Hawai‘i at Manoa, Honolulu, HI, 96822, USA. E-mail: ralfk@hawaii.edu

<sup>b</sup> NASA Astrobiology Institute, University of Hawai‘i at Manoa, Honolulu, HI 96822, USA

timescales. Here, ozone has been identified by ultraviolet reflectance spectroscopy on the surfaces of Ganymede,<sup>16</sup> Rhea, and Dione,<sup>17</sup> trapped within the uppermost surface layers of the water-ice crust.

The processing of astrophysical ices *via* interaction with energetic particles has been the center of considerable experimental investigation over the past decade. A main objective of such studies is to unravel the processes that chemically modify the molecular composition. In the context of the present study, aggregates of carbon dioxide and oxygen molecules implanted in water ice surfaces of outer Solar System bodies are often exposed to a variety of irradiation sources. Galactic cosmic ray (GCR) particles, comprising of about 87% H<sup>+</sup> (protons) and 12% He<sup>2+</sup> ( $\alpha$  particles), intersperse almost isotropically throughout the interstellar medium with kinetic energies,  $E_k$ , peaking at 1 GeV.<sup>18</sup> In the Solar System, small icy bodies are also exposed to radiation from the solar wind (photons, electrons, and ions—about 96% H<sup>+</sup>, 4% He<sup>2+</sup>, and a few heavier nuclei). These particles possess kinetic energies of the order of  $\sim 1$  keV per amu, considerably less than GCRs.<sup>18</sup> In addition, the surfaces of the gas giant satellites continually interact with plasmas consisting of ions ( $E_k \approx 1$ –500 eV per amu), charged particles of a few keV, and electrons. These species are captured and accelerated in the Jupiter and Saturn magnetospheres, which expand to encompass the orbiting path of many of their icy moons.

Experimental studies simulating energetic (keV) electron bombardment of pure carbon dioxide condensates have been performed at 10 K.<sup>19,20</sup> Here, the on-line and *in situ* analysis of the irradiated ices by Fourier-transform infrared spectroscopy (FTIR) detected alterations in the chemical composition of the surface over the exposure period. Mass spectrometry was also employed to observe the molecular products subliming into the gas-phase after the samples were annealed to 300 K. Quantitative analysis of the spectra yielded mechanistic pathways and reaction kinetics for the formation of cyclic carbon trioxide (*c*-CO<sub>3</sub>), while the same experiments confirmed carbon monoxide (CO) and ozone as irradiation products in the ice matrix. By extending the research<sup>21</sup> to perform electron irradiation on condensed carbon oxide (CO, CO<sub>2</sub>, and CO<sub>3</sub>) mixtures, the authors also uncovered the formation of dicarbon monoxide (CCO) and carbon suboxide (C<sub>3</sub>O<sub>2</sub>). In addition, a series of investigations had untangled the formation processes for cyclic, oxygen-rich species carbon tetraoxide (CO<sub>4</sub>),<sup>22</sup> carbon pentaoxide (CO<sub>5</sub>),<sup>23</sup> and carbon hexaoxide (CO<sub>6</sub>)<sup>24</sup> by detecting their infrared signals at 10 K. A similar analytical approach involving the irradiation of pure oxygen ices with energetic electrons<sup>25</sup> uncovered the reaction processes leading to ozone production in the condensate, including an in-depth kinetics investigation for the dissociation and formation pathways. Earlier studies<sup>26,27</sup> irradiating oxygen ices with 100 keV protons (H<sup>+</sup>) also documented the abundance of ozone and its dependence on the fluence of particle irradiation to the surface. Although a similar ozone production model to the electron irradiation experiments was developed,<sup>26</sup> a kinetic analysis of the associated reaction pathways was not performed. Irradiation of pure carbon dioxide ices with 15–100 keV H<sup>+</sup> and helium ions (He<sup>+</sup>) has also been recently studied at 16 K.<sup>28</sup> Here, implantation of the impinging H<sup>+</sup> ions resulted

in the formation of carbonic acid (H<sub>2</sub>CO<sub>3</sub>), confirming that the irradiating species not only decomposes the target ice sample through energy transfer but can also participate in the subsequent reactions to form new molecules and chemical bonds. High linear energy transfer (LET) irradiation of 13 K carbon dioxide ices with 46 MeV <sup>58</sup>Ni<sup>11+</sup> particles, selected to replicate high energy GCR collisions, have also been conducted.<sup>29</sup> These studies determined the total abundances of carbon monoxide, carbon trioxide, and ozone, in addition to the sputtering yield, which was calculated to be  $4.0 \times 10^4$  carbon dioxide molecules ejected from the sample per impact (four orders of magnitude higher than H<sup>+</sup> collisions of the same velocity).

In light of recent advances in the understanding of radiolytic processing of astrophysical ices, the research presented in this work investigates the irradiation of low temperature (12 K) oxygen and carbon dioxide condensates with 5 keV protons and helium ions. By this method, we hope to simulate the reaction mechanisms associated with keV charged particle radiation of icy outer Solar System bodies such as those trapped in the magnetospheres of the giant planets Jupiter and Saturn. As opposed to previous studies, we have chosen to focus on the lower end of the kinetic energy scale for H<sup>+</sup> and He<sup>+</sup> ion radiation. The reason for this is two fold. Firstly, lower energy particles can only penetrate to shallow depths when entering a solid, losing energy through multiple collisions with the ice molecules. As we only condense thin layers ( $\sim 100$ –1000 nm scale) of the condensates, we require the irradiating particle to be fully stopped to achieve a complete transfer of its kinetic energy to the sample. A complete energy transfer enables us to perform accurate calculations on energy dosages and the reaction dynamics of the system. The experimental setup incorporated in the present study uses FTIR and quadrupole mass spectrometry (QMS) to monitor the sample *in situ* and on-line during the irradiation period. The sensitivity of the apparatus allows for molecular precursor and radiolytic product abundances to be calculated as they are formed, leading to the reaction rates to be determined for the systems. Secondly, we are interested to see if implanted hydrogen ions react once their translational energy is sufficiently diminished, as thermal or suprathreshold (few eV) particles can react with the surrounding molecules. This is expected to lead to profound differences in H<sup>+</sup> and He<sup>+</sup> ion irradiation experiments, as helium cannot form stable chemical bonds, but neutralized hydrogen atoms can. By comparing the results of the ion implantations with electron exposures studied previously, we also can quantify to what extent electronic ( $S_e$ ) and nuclear energy loss transfer processes ( $S_n$ ) can lead to chemical alterations of the target molecules.

## Experimental

### Experimental setup

The top view of the experimental setup is depicted in Fig. 1. A contamination-free stainless steel chamber (volume = 15 L) was evacuated to ultrahigh vacuum (UHV) conditions ( $6.5 \times 10^{-11}$  Torr) using an oil-free magnetically suspended

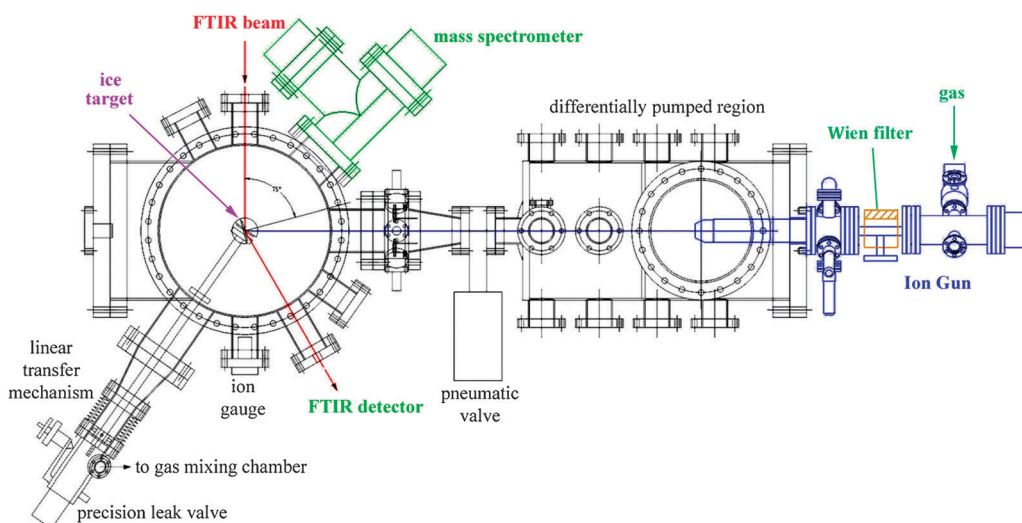


Fig. 1 Top view of the experimental setup.

turbo-pump which was backed with an oil-free scroll pump. Suspended vertically from the top of the chamber and allowed to rotate freely through the use of a differentially pumped feed-through, the cold-head of a two stage, closed-cycle helium refrigerator (CTI-Cryogenics CP-1020) held a polished, silver wafer. Attached to the end of the cold-head to serve as a substrate for the condensed ice samples, the temperature of the silver wafer reached  $11.9 \pm 0.5$  K under UHV conditions measured by a silicon diode sensor (Lakeshore DT-470). For the gas condensation, BOC Gases Grade 5.0 oxygen and carbon dioxide cylinders were connected *via* a gas mixing chamber to a precision leak valve; the latter was attached to a linear transfer arm which was used to locate the deposition gas nozzle 10 mm in front of the substrate. The leak valve was then opened so that the pressure in the main chamber reached  $1.0 \times 10^{-8}$  Torr over a deposition time period of 20 minutes for oxygen condensation and a pressure of  $1.0 \times 10^{-7}$  Torr for 2 minutes for carbon dioxide condensation. The purity of the gases of oxygen and carbon dioxide were monitored on-line *via* a Balzer QMG 420 QMS operating in residual gas analyzer mode (electron impact energy of 100 eV at a 0.3 mA emission current). After condensation, a Nicolet 6700 FTIR was used to record a spectrum of the 6000–400  $\text{cm}^{-1}$  mid-infrared (mid-IR) region of the condensate. Each spectrum was collated from 196 individual scans at a resolution of 2  $\text{cm}^{-1}$ .

The thicknesses of the oxygen and carbon dioxide ice samples which were produced by the specific deposition conditions detailed above were measured using mass spectrometry.<sup>30,31</sup> Briefly, following the condensation of the ice samples at 12 K (with the chamber returned to UHV pressure) the substrate was heated to 300 K. Annealing to 300 K not only allowed for the detection of the ice molecules subliming from the silver substrate (first stage—initially 10 K), but also the fraction of molecules that have re-condensed on the second stage of the cold head and its attached copper heat shield ( $\sim 60$  K without heating). In the case of carbon dioxide, re-condensed species are observed to sublime only as the heat load supplied by the cartridge heater is high enough to warm the second stage components of the cold head above 95 K.<sup>19</sup> The profiles of the

singularly ionized oxygen ( $\text{O}_2^+$ :  $m/z = 32$ ) and carbon dioxide ( $\text{CO}_2^+$ :  $m/z = 44$ ) species were recorded by the QMS, as well as their dissociative ionization products (*i.e.*  $\text{O}^+$ :  $m/z = 16$ ) produced from electron impact in the ionizer. The ion currents recorded for oxygen ( $1.68 \pm 0.05 \times 10^{-3}$  A s) and carbon dioxide ( $9.90 \pm 0.08 \times 10^{-5}$  A s), integrated over their respective sublimation periods, were converted to an average pressure of molecular oxygen ( $3.2 \pm 0.1 \times 10^{-7}$  Torr) and carbon dioxide ( $2.7 \pm 0.1 \times 10^{-8}$  Torr) by respectively scaling to data obtained from calibration experiments previously performed in the main chamber. It follows that the total number of molecules comprising of each solid sample can be calculated using the pumping efficiency,  $S_{\text{eff}}$ , of the system ( $950 \text{ L s}^{-1}$  for both  $\text{O}_2$  and  $\text{CO}_2$ —Osaka Vacuum), when assuming real gas conditions. Finally, using literature densities of pure  $\alpha$ -phase solid oxygen ( $1.55 \text{ g cm}^{-3}$ )<sup>32</sup> and solid phase carbon dioxide ( $1.70 \text{ g cm}^{-3}$ ),<sup>33</sup> both at 10 K, the condensate thicknesses were determined to be  $3.7 \pm 0.7 \times 10^3$  nm for the oxygen sample and  $1.6 \pm 0.3 \times 10^2$  nm for the carbon dioxide ice.

### Ion source

Once the oxygen and carbon dioxide ices were characterized, they were ready to be irradiated isothermally at 12 K by either 5 keV protons ( $\text{H}^+$ ) or helium ( $\text{He}^+$ ) ions.  $\text{H}^+$  and  $\text{He}^+$  were produced separately by feeding  $5.0 \times 10^{-4}$  Torr of either high purity molecular hydrogen ( $\text{H}_2$ : 99.9999%; Mattheson) or helium ( $\text{He}$ : 99.9999%; Airgas) gas into the source chamber of an ion source (SPECS IQE 12/38). Here, the gas was ionized *via* electron impact to produce a plasma containing the  $\text{H}^+$  or  $\text{He}^+$  ions. These ions were then accelerated to a kinetic energy of 5 keV by an extraction potential. Connected to the ion source is a Wien mass filter (SPECS WF-IQE) fitted with a 0.12 Tesla magnet; this allowed for the selection of particles with a specific mass-to-charge ratio, in the range of 0.2–50 amu. This was performed by altering the voltage across a set of internal deflection plates. This effectively removed any unwanted ions produced in the plasma, such as  $\text{H}_2^+$ ,  $\text{H}_3^+$ ,

and  $\text{He}^{2+}$ , from the ion beams. Therefore, the respective beams contained solely mono-energetic  $\text{H}^+$  and  $\text{He}^+$ . A series of focusing lenses and deflection plates directed the beam toward the substrate in the main experimental chamber. A distance of 660 mm from the ion source to the substrate required four differential pumping stages (Fig. 1) and a series of apertures for the passage of the ions. The series of magnetically suspended turbo-pumps and differential pumping chambers reduced the pressure from  $5.0 \times 10^{-4}$  Torr (source chamber) to  $1.0 \times 10^{-10}$  Torr in the main chamber to uphold the UHV conditions during the irradiation experiment.

To monitor the ion current and the beam profile, a Faraday cup (Kimball Physics FC-70C) with an opening of  $0.02 \text{ cm}^2$  was mounted on a linear transfer arm between the source and the substrate. This was connected *via* an electrical feed-through to a picoammeter (Keithly 480). For the  $\text{H}^+$  and  $\text{He}^+$  irradiations, beam currents of  $1.8 \pm 0.4 \text{ nA}$  and  $130 \pm 25 \text{ nA}$  were determined. Since the aperture of the Faraday cup was smaller than the diameter of the ion beam, a second Faraday cup was also mounted onto the target to measure the integrated ion current. For the  $\text{H}^+$  irradiation, a beam current of  $19 \pm 4 \text{ nA}$  was measured, while for  $\text{He}^+$  irradiation, a higher beam current of  $290 \pm 52 \text{ nA}$  was obtained. In addition, the beam exposure to the substrate covered an area of  $0.50 \pm 0.06 \text{ cm}^2$  in both instances. For the oxygen and carbon dioxide ice irradiation experiments, the  $\text{H}^+$  and  $\text{He}^+$  exposure periods were dependent on the time necessary to observe a saturation level in the temporal profiles of the products detected by FTIR. Once changes in the FTIR and QMS spectra had been observed to stabilize with continued exposure time, the ion source was switched off and the irradiated ice was left to stand over a 30 minute period. The ice samples were then heated to 300 K (at a rate  $0.5 \text{ K min}^{-1}$ ) using the temperature control unit (Lakeshore 331) and a 50  $\Omega$  cartridge heater attached to the cold head. This enabled the identification of all volatile species in the irradiated ice composition at their specific sublimation points under the experimental conditions.

The penetration depth (Table 1) for 5 keV ions entering an oxygen ice sample, of density  $1.55 \text{ g cm}^{-3}$ , was calculated to be  $137 \pm 7 \text{ nm}$  for  $\text{H}^+$  irradiation and  $77 \pm 4 \text{ nm}$  for  $\text{He}^+$  irradiation, using the SRIM Monte Carlo program<sup>34</sup> for the projected ranges of ions in solids. For carbon dioxide ice of a density  $1.70 \text{ g cm}^{-3}$ , the stopping range for  $\text{H}^+$  was calculated to be  $113 \pm 6 \text{ nm}$ , while  $\text{He}^+$  ions were determined to have a penetration depth of  $65 \pm 3 \text{ nm}$ . In all cases, the stopping range of the impinging ions is less than the total thickness of the condensed ice, allowing for the complete transfer of the kinetic energy of the impinging ion to the sample. The total energy,  $E(\text{H}^+)$  and  $E(\text{He}^+)$  supplied by the ion irradiation was determined using the parameters summarized in

Table 1. Here, 5 keV  $\text{H}^+$  ions irradiated with a beam current of  $I(\text{H}^+) = 19 \pm 4 \text{ nA}$  over the exposure time,  $t$  (s), yields a total transmitted energy,  $E(\text{H}^+)$ , of  $4.2 \pm 0.7 \times 10^{19} \text{ eV}$  for oxygen ice and  $0.9 \pm 0.2 \times 10^{19} \text{ eV}$  for carbon dioxide ice. In addition, the total energy transmitted to the ice samples by 5 keV  $\text{He}^+$  irradiation ( $I(\text{He}^+) = 290 \pm 52 \text{ nA}$ ) is  $7.5 \pm 0.9 \times 10^{19} \text{ eV}$  for oxygen ice and  $1.4 \pm 0.4 \times 10^{19} \text{ eV}$  for carbon dioxide ice.

It follows that the average *Dose* ( $\text{eV molecule}^{-1}$ ) of energy absorbed by an individual molecule in the ice samples can be obtained. These values are calculated to be  $209 \pm 71 \text{ eV molecule}^{-1}$  for  $\text{H}^+$  and  $672 \pm 198 \text{ eV molecule}^{-1}$  for  $\text{He}^+$  irradiating an oxygen ice sample. The average *Dose* for each molecule in a carbon dioxide ice sample is calculated to be  $68 \pm 29 \text{ eV molecule}^{-1}$  for  $\text{H}^+$  and  $184 \pm 80 \text{ eV molecule}^{-1}$  for  $\text{He}^+$ . In comparison to the strength of the oxygen double bond in molecular oxygen (5.1 eV) and the carbon–oxygen double bond in molecular carbon dioxide (8.1 eV), the *doses* absorbed by each molecule is sufficient to promote the breaking of molecular bonds in the sample.

## Results

### Qualitative analysis

**Infrared spectroscopy.** The baseline corrected FTIR spectra obtained from pristine oxygen ice and the same ice sample after exposure to  $\text{H}^+$  at 12 K is depicted in Fig. 2a. Here, the

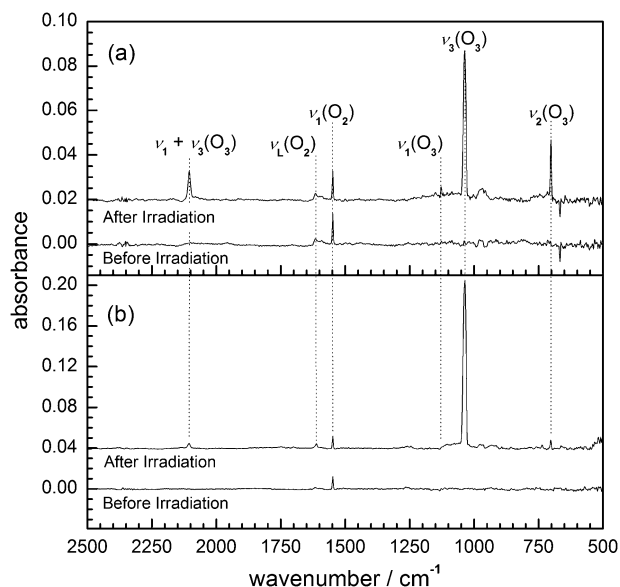


**Fig. 2** Mid-IR spectra of molecular oxygen ice before and after (a)  $\text{H}^+$  and (b)  $\text{He}^+$  irradiation at 12 K. Absorption band positions and assignments are presented in Table 2.

**Table 1** Experimental irradiation parameters

| Ice           | Ion           | Density/ $\text{g cm}^{-3}$ | Penetration depth/nm | Exposure time/s | Transmitted energy ( $\times 10^{19} \text{ eV}$ ) | Average dose/ $\text{eV molecule}^{-1}$ |
|---------------|---------------|-----------------------------|----------------------|-----------------|--|---|
| $\text{O}_2$  | $\text{H}^+$  | 1.55                        | $137 \pm 7$          | 73 800          | $4.2 \pm 0.7$                                      | $209 \pm 71$                            |
|               | $\text{He}^+$ |                             | $77 \pm 4$           | 7200            | $7.5 \pm 0.9$                                      | $672 \pm 198$                           |
| $\text{CO}_2$ | $\text{H}^+$  | 1.70                        | $113 \pm 6$          | 14 400          | $0.9 \pm 0.2$                                      | $68 \pm 29$                             |
|               | $\text{He}^+$ |                             | $65 \pm 3$           | 1800            | $1.4 \pm 0.4$                                      | $184 \pm 80$                            |

**Table 2** Absorption bands and assignments of molecular oxygen ices

| Absorbance/cm <sup>-1</sup> | H <sup>+</sup> irradiation absorbance/cm <sup>-1</sup> | He <sup>+</sup> irradiation absorbance/cm <sup>-1</sup> | Assignment <sup>a</sup>       | Characterization   |
|-----------------------------|--|---|-------------------------------|--------------------|
|                             | 702  | 702   | $\nu_2(\text{O}_3)$           | Bending            |
|                             | 1038   | 1036  | $\nu_3(\text{O}_3)$           | Asymmetric stretch |
|                             | 1128   | —   | $\nu_1(\text{O}_3)$           | Symmetric stretch  |
| 1548                        |  |   | $\nu_1(\text{O}_2)^b$         | Stretching         |
| 1614                        |  |   | $\nu_1 + \nu_L(\text{O}_2)^b$ | Lattice mode       |
|                             | 2105   | 2106  | $\nu_1 + \nu_3(\text{O}_3)$   | Combination band   |

<sup>a</sup> Brewer and Wang (1972). <sup>b</sup> Freiman and Jodl (2004).

pristine oxygen spectrum clearly shows the 1548 cm<sup>-1</sup> absorption band attributed to the  $\nu_1(\text{O}_2)$  stretching mode of solid-state molecular oxygen,<sup>32</sup> which is perturbed in the amorphous ice composition to become IR active. In addition, a broad, low intensity absorption band centered at 1614 cm<sup>-1</sup> can be assigned to a combination band of the fundamental with the lattice vibrations of molecular oxygen,  $\nu_1 + \nu_L(\text{O}_2)$ . The observation of these bands suggests that there are regions of ordered, crystalline structure within a predominantly amorphous oxygen ice sample. The irradiation of the oxygen with H<sup>+</sup> results in the formation of molecular ozone (O<sub>3</sub> X<sup>1</sup>A<sub>1</sub>), displaying a bent C<sub>2v</sub> structure. The species is identified by four absorption features in the mid-IR region (Table 2) previously assigned in the literature.<sup>35</sup> These are the three fundamental bands of ozone; the weak 1128 cm<sup>-1</sup>  $\nu_1(\text{O}_3)$  symmetric stretching vibration, the low frequency  $\nu_2(\text{O}_3)$  bending vibration at 702 cm<sup>-1</sup>, and the 1038 cm<sup>-1</sup>  $\nu_3(\text{O}_3)$  asymmetric stretching vibration. In addition, the  $\nu_1 + \nu_3(\text{O}_3)$  combination band is also clearly identified at 2105 cm<sup>-1</sup>.

Depicted in Fig. 2b is the mid-IR spectrum of oxygen ice recorded after 2 hours of He<sup>+</sup> ion irradiation at 12 K. Here, evidence is also provided for the formation of ozone through

the identification of the same set of absorption bands observed in the H<sup>+</sup> experiment (Table 2). As the He<sup>+</sup> irradiation transfers a higher total energy to the oxygen condensate than the H<sup>+</sup> irradiation, the intensity of the 1038 cm<sup>-1</sup>  $\nu_3(\text{O}_3)$  asymmetric stretching vibration is seen to increase. However, the 702 cm<sup>-1</sup>  $\nu_2(\text{O}_3)$  bending vibration and the 2105 cm<sup>-1</sup>  $\nu_1 + \nu_3(\text{O}_3)$  combination band both display similar intensities to those recorded after H<sup>+</sup> irradiation. The 1128 cm<sup>-1</sup>  $\nu_1(\text{O}_3)$  symmetric stretching vibration is not observed in the He<sup>+</sup> spectrum.

Switching attention to the FTIR spectra of carbon dioxide ices, Fig. 3a and b display the baseline corrected mid-IR spectrum collected after four hours of exposure to H<sup>+</sup> irradiation at 12 K. The mid-IR absorption bands attributed to the linear, ground state carbon dioxide molecule (CO<sub>2</sub> X<sup>1</sup>Σ<sub>g</sub><sup>+</sup>) are observed and are in agreement with the literature values (Table 3).<sup>36</sup> Specifically, absorption bands for the  $\nu_2(\text{CO}_2)$  bending fundamental at 654 cm<sup>-1</sup> and the  $\nu_3(\text{CO}_2)$  asymmetric stretching fundamental at 2339 cm<sup>-1</sup> are readily identified. The  $2\nu_2 + \nu_3(\text{CO}_2)$  and  $\nu_1 + \nu_3(\text{CO}_2)$  combination bands are also located at 3600 cm<sup>-1</sup> and 3709 cm<sup>-1</sup> respectively. In addition, the absorption band at 2283 cm<sup>-1</sup> can be assigned to

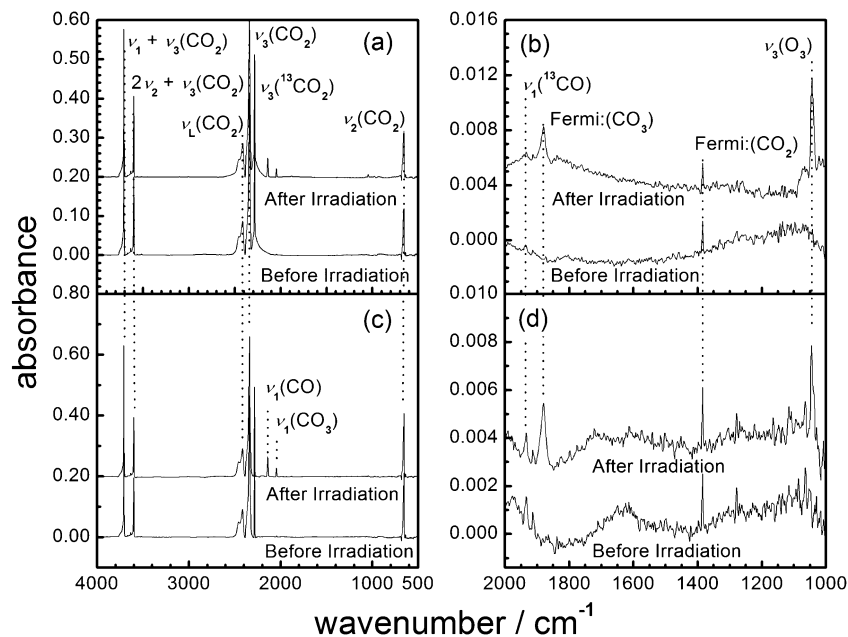


**Fig. 3** Mid-IR spectra of carbon dioxide ice before and after (a and b) H<sup>+</sup> irradiation and (c and d) He<sup>+</sup> irradiation at 12 K. Absorption band positions and assignments are presented in Table 3.

**Table 3** Absorption band positions and assignments of carbon dioxide ices

| Absorbance/cm <sup>-1</sup> | H <sup>+</sup> irradiation absorbance/cm <sup>-1</sup> | He <sup>+</sup> irradiation absorbance/cm <sup>-1</sup> | Assignment <sup>a</sup>             | Characterization           |
|-----------------------------|--|---|-------------------------------------|----------------------------|
| 654                         |  |   | $\nu_2(\text{CO}_2)$                | In-plane/out-of-plane bend |
|                             | 1045   | 1045  | $\nu_3(\text{O}_3)^b$               | Asymmetric stretch         |
| 1384                        |  |   | Fermi( $\text{CO}_2$ )              | Fermi resonance            |
|                             | 1879   | 1880  | Fermi( $\text{CO}_3$ ) <sup>b</sup> | Fermi resonance            |
|                             | 2044   | 2044  | $\nu_1(\text{CO}_3)^b$              | CO stretch                 |
|                             | —  | 2091  | $\nu_1(^{13}\text{CO})^b$           | Isotope peak               |
|                             | 2140   | 2140  | $\nu_1(\text{CO})^b$                | Stretching                 |
| 2283                        |  |   | $\nu_3(^{13}\text{CO}_2)$           | Isotope peak               |
| 2339                        |  |   | $\nu_3(\text{CO}_2)$                | Asymmetric stretch         |
| 2412                        |  |   | $\nu_3 + \nu_L(\text{CO}_2)$        | Lattice mode               |
| 3600                        |  |   | $2\nu_2 + \nu_3(\text{CO}_2)$       | Combination band           |
| 3709                        |  |   | $\nu_1 + \nu_3(\text{CO}_2)$        | Combination band           |

<sup>a</sup> Sandford and Allamandola (1990). <sup>b</sup> Bennett *et al.* (2004).

the  $\nu_3(^{13}\text{CO}_2)$  asymmetric stretch of the <sup>13</sup>C isotopic analogue of carbon dioxide. Finally, positioned at 2412 cm<sup>-1</sup>, the prominent lattice mode  $\nu_3 + \nu_L(\text{CO}_2)$  absorption feature is identified.

The H<sup>+</sup> irradiation of the carbon dioxide ice produces a number of absorption features that can be attributed to the formation of new species. Carbon monoxide is identified by the intense band positioned at 2140 cm<sup>-1</sup> which is attributed to its lone  $\nu_1(\text{CO})$  stretching fundamental. The formation of carbon trioxide ( $\text{CO}_3$ ) is confirmed by its  $\nu_1(\text{C}=\text{O})$  stretching fundamental positioned at 2044 cm<sup>-1</sup>. Furthermore, the absorption feature positioned at 1879 cm<sup>-1</sup> is assigned as a Fermi resonance band caused by vibrational mixing of the  $\nu_1(\text{C}=\text{O})$  mode and the first overtone of the  $\nu_5(\text{C}-\text{O})$  stretching mode, which is not identified in the spectrum at its ~970 cm<sup>-1</sup> position. The appearance of the Fermi resonance band also identifies the specific isomer of the carbon trioxide product as the cyclic structure, following that the Fermi absorption band is only activated in the  $C_{2v}$  symmetric molecule, as opposed to the  $C_s$  or  $D_{3h}$  symmetric structures of carbon trioxide.<sup>19</sup> Finally, ozone was also detected by assignment of its 1045 cm<sup>-1</sup>  $\nu_3(\text{O}_3)$  asymmetric stretching vibration.

For the mid-IR spectrum obtained from 12 K carbon dioxide ice (Fig. 3c and d), after being irradiated with 5 keV He<sup>+</sup> ions for 30 minutes, the same set molecular products were identified as those produced by the H<sup>+</sup> irradiation experiment (Table 3). Carbon monoxide formation was confirmed by observation of its  $\nu_1(\text{CO})$  mode at 2140 cm<sup>-1</sup>, together with the absorption band for the <sup>13</sup>C isotopic analogue stretching vibration positioned at 2091 cm<sup>-1</sup>. Cyclic, symmetric carbon trioxide was identified by its  $\nu_1(\text{CO}_3)$  band at 2044 cm<sup>-1</sup> and the Fermi resonance feature at 1880 cm<sup>-1</sup>. In addition, molecular ozone was assigned by the  $\nu_3(\text{O}_3)$  symmetric stretch vibration of the species located at 1045 cm<sup>-1</sup>.

In summary, the FTIR on-line analysis of the H<sup>+</sup> and He<sup>+</sup> irradiated molecular oxygen ( $\text{O}_2$ ) condensates identified the formation of newly formed ozone ( $\text{O}_3$ ); the exposed carbon dioxide ( $\text{CO}_2$ ) ices also displayed absorption features attributed to ozone ( $\text{O}_3$ ), in addition to bands assigned to carbon monoxide (CO) and cyclic carbon trioxide (*c*- $\text{CO}_3$ ).

**Mass spectrometry.** Following the irradiation procedure, the substrate is annealed at a rate 0.5 K min<sup>-1</sup> to 300 K. This heating promotes the diffusion of reactive species in the ices

at low temperatures and the sublimation of the ice molecules (molecular oxygen and carbon dioxide) and irradiation products (ozone and carbon monoxide) at specific temperatures under UHV. For the present set of experiments, mass-to-charge (*m/z*) signals are detected as the gas phase molecules sublime from the irradiated ices and are ionized by the QMS, producing an ion current (*A*) which correlates to the species gas-phase abundance. These ion currents are presented as a function of substrate temperature (Fig. 4—line format) and are compared to the blank ice samples (Fig. 4—dotted format). Mass profiles were also recorded during the irradiation phase of the 12 K condensates. However, as the sublimation of all volatile species was suppressed at this temperature, the corresponding mass profiles are not presented.

The ion currents produced from the annealed oxygen ice sample, after the H<sup>+</sup> ion exposure, are displayed in Fig. 4a. Here, molecular hydrogen ( $\text{H}_2^+$ ; *m/z* = 2) is observed to

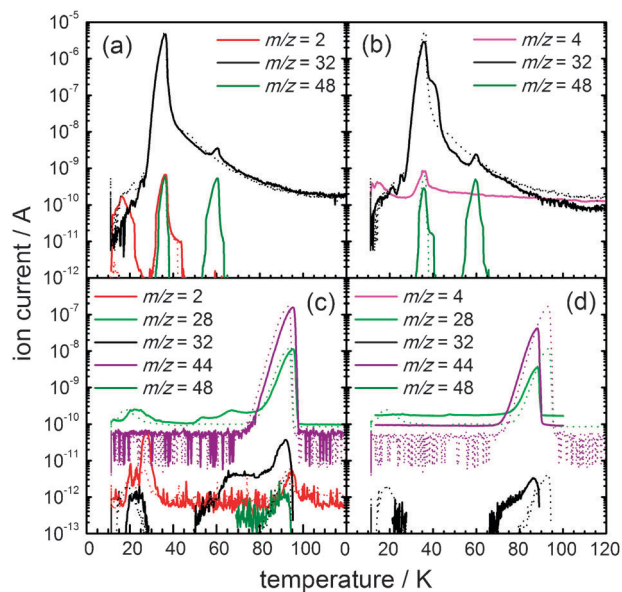


**Fig. 4** Ion currents for gas phase species sublimating during the annealing of molecular oxygen ice after (a) H<sup>+</sup> and (b) He<sup>+</sup> irradiation and of carbon dioxide ice after (c) H<sup>+</sup> and (d) He<sup>+</sup> irradiation. The ion currents for pristine oxygen and carbon dioxide ice samples are included as dotted lines.

sublime between 15 and 25 K. This indicates that the irradiating protons predominantly undergo neutralization to produce hydrogen atoms, which then undergo recombination to form molecular hydrogen ( $\text{H}_2$ ). The molecular oxygen condensate itself ( $\text{O}_2^+$ :  $m/z = 32$ ) starts to sublime at 25 K, also releasing the remaining molecular hydrogen. Molecular ozone ( $\text{O}_3^+$ :  $m/z = 48$ ) is observed to be retained on the substrate before subliming between 55 and 65 K as indicated by previous experiments.<sup>25</sup> The ion profiles for the oxygen ice sample irradiated with  $\text{He}^+$  is shown in Fig. 4b where the ( $\text{He}^+$ :  $m/z = 4$ ) ion current is attributed to the irradiating  $\text{He}^+$  ions implanted in the condensate. In addition, the mass profile for molecular oxygen ( $\text{O}_2^+$ :  $m/z = 32$ ) shows a peak at 35 K, while the ion current for ozone ( $\text{O}_3^+$ :  $m/z = 48$ ) is seen to peak at  $\sim 60$  K.

For the irradiation of carbon dioxide ice with  $\text{H}^+$  ions (Fig. 4c), the ion current for carbon dioxide ( $\text{CO}_2^+$ :  $m/z = 44$ ) displays its sublimation between 80 and 95 K. Molecular hydrogen ( $\text{H}_2^+$ :  $m/z = 2$ ) is observed to sublime in the 20–30 K temperature range. The ion current for  $m/z = 28$  differs from the blank profile by an increase in ion current starting at 50 K, which can be attributed to the sublimation of carbon monoxide ( $\text{CO}^+$ :  $m/z = 28$ ).<sup>21</sup> The slow increase of carbon monoxide toward the carbon dioxide sublimation temperature at 80 K infers a slow diffusion of carbon monoxide through the matrix. In addition, a small amount of ozone ( $\text{O}_3^+$ :  $m/z = 48$ ) is observed to sublime with the carbon dioxide between 80 and 95 K. The mass profiles for the annealed carbon dioxide ice exposed to  $\text{He}^+$  ions are observed in Fig. 4d. Here, the mass fragments ( $m/z = 16, 28$  and 44) attributed to the carbon dioxide condensate were observed after its sublimation at 75 K. There was a slight rise in the ( $\text{CO}^+$ :  $m/z = 28$ ) ion current above its baseline level at  $\sim 50$  K to indicate a small amount of carbon monoxide out-gassing from the ice. However, there was no detection of the ( $\text{O}_3^+$ :  $m/z = 48$ ) ion current at  $\sim 60$  K to suggest ozone formation. It should be noted that  $\sim 52\%$  of ozone undergoes dissociative ionization to form  $\text{O}_2^+$ , which is detected in the ion profile, instead of  $\text{O}_3^+$  after impact with 100 eV electrons in the residual gas analyzer.<sup>37</sup> Therefore, the non-detection of ozone in the QMS suggests that only a small amount of ozone is formed. The cyclic carbon trioxide species (*c*- $\text{CO}_3$ ), previously identified in the solid-state by FTIR, undergoes thermal decomposition at  $\sim 90$  K<sup>20</sup> in the carbon dioxide matrix and is therefore not detected in the gas-phase by QMS. Of final importance for the  $\text{H}^+$  irradiation experiments, mass signals corresponding to primary ionization fragments of hydrogenated species such as water ( $\text{H}_2\text{O}^+$ :  $m/z = 18$ ), hydrogen peroxide ( $\text{H}_2\text{O}_2^+$ :  $m/z = 34$ ), and formaldehyde ( $\text{H}_2\text{CO}^+$ :  $m/z = 30$ ) were programmed into the QMS for detection. However, the evolution of these species in the gas-phase at their specific sublimation temperatures could not be verified due to ion counts below the background level within the chamber (for water) or counts below the  $10^{-14}$  A sensitivity limit of the QMS (for hydrogen peroxide and formaldehyde).

To summarize the results from QMS analysis, the oxygen ice irradiated with  $\text{H}^+$  produced mass profiles attributed to the release of newly formed molecular hydrogen ( $\text{H}_2$ ) and

ozone ( $\text{O}_3$ ), while the sample irradiated with  $\text{He}^+$  inferred the release of atomic helium ( $\text{He}$ ) and ozone ( $\text{O}_3$ ). The  $\text{H}^+$  irradiated carbon dioxide ices released molecular hydrogen ( $\text{H}_2$ ), carbon monoxide ( $\text{CO}$ ), and ozone ( $\text{O}_3$ ) during sublimation, while the samples irradiated with  $\text{He}^+$  only confirmed the formation of carbon monoxide ( $\text{CO}$ ); molecular ozone is below the detection limits due to reasons as outlined above.

## Quantitative analysis

**Oxygen ice.** The irradiation of oxygen with both  $\text{H}^+$  and  $\text{He}^+$  resulted in the formation of molecular ozone. For ozone to form, the ion irradiation must induce homolytic bond cleavage of the molecular oxygen resulting in two oxygen atoms. This should lead to a decrease in the molecular oxygen column density in the sample. This was monitored by the integrated area of the  $\nu_1(\text{O}_2)$  stretching absorption band at  $1548\text{ cm}^{-1}$  in both cases. Using an integral absorption coefficient of  $5.0 \times 10^{-21}\text{ cm molecule}^{-1}$ ,<sup>38</sup> the temporal profiles for the resultant column densities of oxygen irradiated by  $\text{H}^+$  and  $\text{He}^+$  are displayed in Fig. 5 (top). However, the calculated column densities for oxygen do not appear to significantly decrease over the exposure period as a large error is observed between the peak areas in successive spectra taken during the on-line analysis. The initial column density for molecular oxygen,  $[\text{O}_2]_0$ , was calculated to be  $3.8 \pm 0.2 \times 10^{18}$  molecules  $\text{cm}^{-2}$  in the condensate exposed to  $\text{H}^+$  ions and  $3.6 \pm 0.2 \times 10^{18}$  molecules  $\text{cm}^{-2}$  for the condensate in the  $\text{He}^+$  irradiation experiment.

As oxygen molecules are dissociated over the irradiation period, molecular ozone is observed to be the sole product from the reaction between oxygen atoms and the molecular oxygen condensate. This reaction increases the concentration of ozone in the ice samples, as seen by the increase in column density for ozone in Fig. 5 (bottom). The most intense absorption band for ozone in the mid-IR; the  $1045\text{ cm}^{-1}$   $\nu_3(\text{O}_3)$  asymmetric stretching fundamental, was used to calculate these column densities using an integral absorption

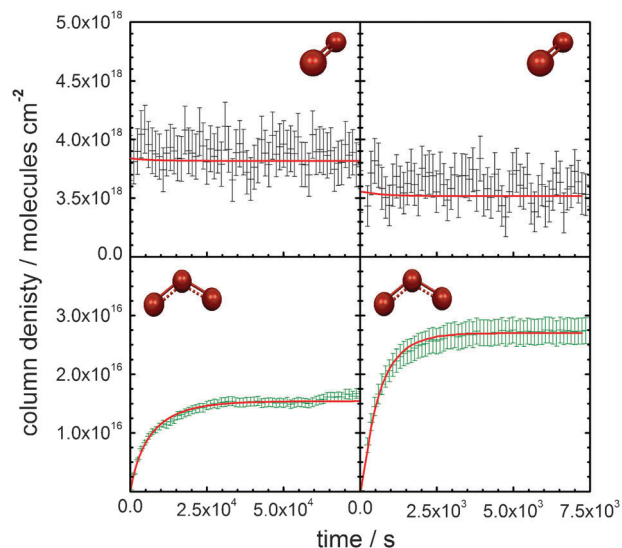


**Fig. 5** Temporal profiles of oxygen and ozone during the irradiation of oxygen ice samples with  $\text{H}^+$  ions (left) and  $\text{He}^+$  ions (right).

coefficient of  $1.5 \times 10^{-17}$  cm molecule $^{-1}$ .<sup>39</sup> It can be observed in the ozone temporal profiles constructed for both the H<sup>+</sup> and He<sup>+</sup> irradiation experiments that, after a period of ozone formation ( $2.5 \times 10^4$  s for H<sup>+</sup> and  $2.5 \times 10^3$  s for He<sup>+</sup>), the abundance of ozone in the ice appears to reach an upper limit. For H<sup>+</sup> irradiation this maximum column density for ozone,  $[\text{O}_3]_{\infty}$ , is  $1.5 \pm 0.1 \times 10^{16}$  molecules cm $^{-2}$  while for He<sup>+</sup> irradiation the maximum column density of ozone is  $2.7 \pm 0.1 \times 10^{16}$  molecules cm $^{-2}$ .

**Carbon dioxide ice.** Processing of carbon dioxide ice samples resulted in the detection of carbon monoxide, cyclic carbon trioxide, and ozone by the identification of their characteristic absorption bands in the mid-IR spectra (Fig. 3). Firstly, the column density of carbon dioxide was calculated from the  $3600 \text{ cm}^{-1} 2\nu_2 + \nu_3(\text{CO}_2)$  and the  $3709 \text{ cm}^{-1} \nu_1 + \nu_3(\text{CO}_2)$  combination bands. For these calculations, the integral absorption coefficients used for the calculations were  $A_{\text{exp}}(3600 \text{ cm}^{-1}) = 4.5 \times 10^{-19}$  cm molecule $^{-1}$  and  $A_{\text{exp}}(3709 \text{ cm}^{-1}) = 1.4 \times 10^{-18}$  cm molecule $^{-1}$ .<sup>40</sup> Temporal profiles constructed for the carbon dioxide column densities over the respective irradiation periods are displayed in Fig. 6. The initial column densities of carbon dioxide,  $[\text{CO}_2]_0$ , are observed to be  $3.8 \pm 0.2 \times 10^{18}$  molecules cm $^{-2}$  and  $4.1 \pm 0.2 \times 10^{18}$  molecules cm $^{-2}$  for the condensates produced for the H<sup>+</sup> and He<sup>+</sup> irradiation experiments respectively.

The bombardment of the ices with fast H<sup>+</sup> and He<sup>+</sup> ions results in the homolytic cleaving of a carbon dioxide molecular bond to produce a carbon monoxide molecule and an oxygen atom. Subsequently, the abundance of carbon monoxide in the ice increases. This growth is monitored by the carbon

monoxide column density after conversion of its  $2140 \text{ cm}^{-1} \nu_1(\text{CO})$  stretching absorption band, using an integrated absorption coefficient of  $1.1 \times 10^{-17}$  cm molecule $^{-1}$ .<sup>41</sup> The abundances of the carbon monoxide species does not reach an upper limit during the exposure periods for both H<sup>+</sup> (4 hours) and He<sup>+</sup> (0.5 hours). Reaction between the newly formed oxygen atom and the initial carbon dioxide species results in the formation of carbon trioxide, which is monitored by its  $2044 \text{ cm}^{-1} \nu_1(\text{CO}_3)$  stretching fundamental. Applying an integral absorption coefficient of  $8.9 \times 10^{-17}$  cm molecule $^{-1}$ <sup>19</sup> to calculate the carbon trioxide column densities, the temporal profile of the species is displayed in Fig. 6. For both H<sup>+</sup> and He<sup>+</sup> irradiation, a quick rise in abundance is observed after the start of irradiation before reaching a maximum abundance further into the exposure period. For the H<sup>+</sup> irradiation experiment, the maximum column density of carbon trioxide,  $[\text{CO}_3]_{\infty}$ , appears to be approaching  $1.2 \pm 0.1 \times 10^{15}$  molecules cm $^{-2}$  after  $6.5 \times 10^3$  s of exposure. However, for the He<sup>+</sup> experiment a maximum column density of  $1.0 \pm 0.1 \times 10^{15}$  molecules cm $^{-2}$  is rapidly obtained after only 500 s of exposure.

Finally, the formation of molecular ozone in carbon dioxide ices irradiated by both H<sup>+</sup> and He<sup>+</sup> is confirmed by the observation of its  $1045 \text{ cm}^{-1} \nu_3(\text{O}_3)$  asymmetric stretching vibration in the mid-IR spectra. Column densities of the ozone component of the processed ices are calculated using the same  $1.5 \times 10^{-17}$  cm molecule $^{-1}$  integral absorption coefficient used for ozone formation in the oxygen ice, allowing for the ozone temporal abundance in the carbon dioxide ice samples to be constructed (Fig. 6). Here, the column density for ozone in the H<sup>+</sup> experiment approaches  $1.2 \pm 0.1 \times 10^{15}$  molecules cm $^{-2}$  over the  $6.5 \times 10^3$  s exposure time. However, the irradiation with He<sup>+</sup> ions produces a maximum ozone column density,  $[\text{O}_3]_{\infty}$ , of  $5.4 \pm 0.3 \times 10^{14}$  molecules cm $^{-2}$ , which is obtained after only 250 s of exposure.

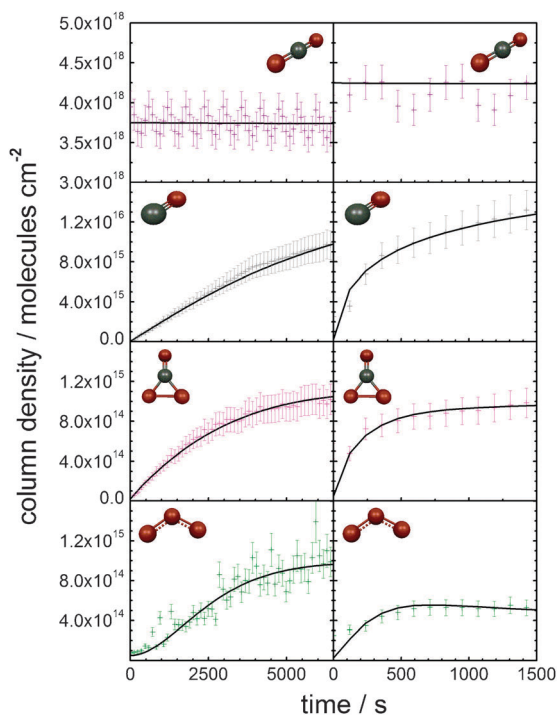


**Fig. 6** Temporal profiles of carbon dioxide, carbon monoxide, carbon trioxide, and ozone during the irradiation of carbon dioxide ice samples with H<sup>+</sup> ions (left) and He<sup>+</sup> ions (right).

## Discussion

### Oxygen ice

**Reaction scheme.** In consideration of the molecular oxygen and ozone temporal profiles discussed above, we propose a reaction scheme with four pathways (Fig. 7) to model the chemical processing of the oxygen ices induced by energetic H<sup>+</sup> and He<sup>+</sup> ion exposure. To calculate the rate constants for the interconnected reactions, a set of four coupled differential equations was constructed to represent each process; these equations were solved simultaneously using a mathematical computation program.<sup>42–44</sup> This approach ensured that no

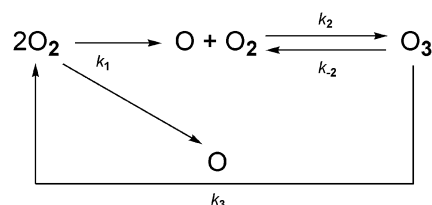


**Fig. 7** Reaction scheme for oxygen ices irradiated with H<sup>+</sup> and He<sup>+</sup> ions.

reaction rate was derived independently from another and that the abundances of all reactants, products, and reaction intermediates were conserved at all times. The optimized fits are displayed in Fig. 5, super-positioned on the column density profiles of each experimentally detected species. Here, the fits are observed to follow the temporal profiles to within a 5% error of the data points. In addition, the abundances of all products were derived directly from the initial column density of the molecular oxygen precursor,  $[O_2]_0$ ; measured to be  $3.8 \pm 0.2 \times 10^{18}$  molecules  $\text{cm}^{-2}$  for the  $H^+$  experiment and  $3.5 \pm 0.2 \times 10^{18}$  molecules  $\text{cm}^{-2}$  for the  $He^+$  experiment.

The devised reaction scheme (Fig. 7) can now be expressed in terms of the chemical processes occurring in the irradiated oxygen ice samples. Upon collision with an impinging ion (or *via* unimolecular decomposition of an oxygen molecule followed by an inelastic energy transfer), an oxygen molecule can be dissociated *via* homolytic bond rupture to form either a pair of ground state oxygen atoms or a ground state oxygen atom and an oxygen atom in the first electronically excited state.<sup>45</sup> This process can be induced *via* a simple unimolecular decomposition of internally excited oxygen (the internal energy is transferred from the keV ion *via* inelastic interaction  $S_e$ ) or by a direct knock-on process (the implant ejects an oxygen atom from the oxygen molecule after a direct collision *via* the nuclear interaction potential  $S_n$ ). This first-order decomposition of molecular oxygen occurs at a rate  $k_1$  ( $\text{s}^{-1}$ ) over the irradiation period and results in the decrease in the oxygen column density observed in Fig. 5. The oxygen atoms are liberated with excess kinetic energy and hence are not in thermal equilibrium with the surrounding ice. This provides the oxygen atoms with sufficient mobility to react with an additional oxygen molecule in the matrix to form an ozone molecule.<sup>25</sup> The production of ozone (evolved at a bimolecular reaction rate  $k_2$  ( $\text{molecules}^{-1} \text{cm}^2 \text{s}^{-1}$ )) correlates with its increase in column density observed in Fig. 5 over the respective exposure periods for  $H^+$  and  $He^+$  ion irradiation. However, as the exposure time increases, the flattening of the ozone temporal profiles suggests its abundance reaches

equilibrium between formation and destruction processes. It was found that two destruction channels were necessary to fit the experimental data. The first of these channels involves the destruction of ozone *via* interaction of an implanted ion. The collision induces ozone to undergo homolytic bond rupture *via* electronic ( $S_e$ ) or nuclear ( $S_n$ ) interaction, forming an oxygen molecule and an oxygen atom at a first-order reaction rate  $k_{-2}$  ( $\text{s}^{-1}$ ). The second destruction pathway involves the bimolecular reaction between a suprathermal oxygen atom and an ozone molecule, resulting in the production of two oxygen molecules at a rate  $k_3$  ( $\text{molecules}^{-1} \text{cm}^2 \text{s}^{-1}$ ).

#### Quantification of rate constants and correlation with $S_e/S_n$ .

To obtain a quantitative measure of the energy transfer processes that occur as energetic particles penetrate an oxygen ice sample, TRansport of Ions in Matter<sup>34</sup> calculations were performed to simulate the kinetic energy loss of the impinging ions before being completely stopped in the solid target; with data averaged over 10 000 ion trajectories (Table 4). We determine that on average, each proton transfers  $27.4 \text{ keV } \mu\text{m}^{-1}$  through inelastic electronic interactions and  $1.3 \text{ keV } \mu\text{m}^{-1}$  by elastic nuclear collisions with oxygen ( $S_n/S_e = 0.05$ ), yielding a total linear energy transfer of  $28.7 \text{ keV } \mu\text{m}^{-1}$ . Similarly for the helium ions, we calculate  $28.3 \text{ keV } \mu\text{m}^{-1}$  of the kinetic energy is dissipated by excitation of target electrons and  $12.6 \text{ keV } \mu\text{m}^{-1}$  is lost *via* nuclear interactions between oxygen and the ion ( $S_n/S_e = 0.45$ ). This gives a total linear energy transfer of  $40.9 \text{ keV } \mu\text{m}^{-1}$ .

The reaction rates derived for the irradiation of oxygen ice with  $H^+$  and  $He^+$  at 12 K are summarized in Table 5. The rate constants for the first-order decomposition oxygen were derived as  $k_1 = 4.0 \pm 0.2 \times 10^{-7} \text{ s}^{-1}$  for  $H^+$  exposure and  $k_1 = 1.8 \pm 0.1 \times 10^{-5} \text{ s}^{-1}$  for the  $He^+$  experiment. The rate calculated for the destruction of oxygen with  $He^+$  compared was calculated to be two orders-of-magnitude faster than that induced by  $H^+$  irradiation. This can be correlated with the difference in energy loss ( $\text{keV } \mu\text{m}^{-1}$ ) of the ions in the oxygen matrix. A combined  $40.9 \text{ keV } \mu\text{m}^{-1}$  is transferred by the  $He^+$

**Table 4** Stopping powers

| Ice    | Ion    | Stopping range/nm | Electronic stopping $S_e/\text{keV } \mu\text{m}^{-1}$ | Nuclear stopping $S_n/\text{keV } \mu\text{m}^{-1}$ | Vacancies per ion | Atomic oxygen abundance/atoms |
|--------|--------|-------------------|--|---|-------------------|-------------------------------|
| $O_2$  | $H^+$  | $137 \pm 7$       | 27.4   | 1.3   | 32.0              | $5.3 \pm 0.9 \times 10^{17}$  |
|        | $He^+$ | $77 \pm 4$        | 28.3   | 12.6  | 148.0             | $4.4 \pm 0.5 \times 10^{18}$  |
| $CO_2$ | $H^+$  | $113 \pm 6$       | 36.1   | 1.5   | 17.2              | $6.2 \pm 1.6 \times 10^{16}$  |
|        | $He^+$ | $65 \pm 3$        | 37.5   | 14.6  | 85.0              | $4.8 \pm 1.2 \times 10^{17}$  |

**Table 5** Kinetic data for molecular oxygen irradiation at 12 K

| Pathway                             | Reaction scheme                    | Rate constants <sup>a</sup>           |                                       |
|-------------------------------------|------------------------------------|---------------------------------------|---------------------------------------|
|                                     |                                    | $H^+$                                 | $He^+$                                |
| $O_2$ destruction                   | $O_2 \xrightarrow{k_1} O + O$      | $k_1 = 4.0 \pm 0.2 \times 10^{-7}$    | $k_1 = 1.8 \pm 0.1 \times 10^{-5}$    |
| $O_2$ destruction/ $O_3$ formation  | $O_2 + O \xrightarrow{k_2} O_3$    | $k_2 = 2.2 \pm 0.1 \times 10^{-21}$   | $k_2 = 3.8 \pm 0.2 \times 10^{-19}$   |
| $O_3$ destruction/ $O_2$ formation  | $O_3 \xrightarrow{k_{-2}} O_2 + O$ | $k_{-2} = 4.9 \pm 0.3 \times 10^{-8}$ | $k_{-2} = 1.1 \pm 0.1 \times 10^{-5}$ |
| $O_3$ destruction/ $2O_2$ formation | $O_3 + O \xrightarrow{k_3} 2O_2$   | $k_3 = 5.5 \pm 0.3 \times 10^{-19}$   | $k_3 = 3.0 \pm 0.2 \times 10^{-17}$   |

<sup>a</sup> Unimolecular reaction rate constants  $k_1$  and  $k_{-2}$  in  $\text{s}^{-1}$  and bimolecular reaction rate constants  $k_2$  and  $k_3$  in  $\text{molecules}^{-1} \text{cm}^2 \text{s}^{-1}$ .

ions by electronic excitation and direct nuclear collisions with the oxygen molecules, compared to  $28.7 \text{ keV } \mu\text{m}^{-1}$  transferred by the  $\text{H}^+$  ions. In addition, the ratio of the nuclear interaction potential to the electronic interaction potential ( $S_n/S_e$ ) is ten fold greater for the more massive  $\text{He}^+$  ions than the  $\text{H}^+$  ions. Subsequently, the rate of ozone generation in the  $\text{He}^+$  experiment ( $k_2 = 3.8 \pm 0.2 \times 10^{-19} \text{ molecules}^{-1} \text{ cm}^2 \text{ s}^{-1}$ ) is two orders-of-magnitude faster than the ozone formation rate in the  $\text{H}^+$  experiment ( $k_2 = 2.2 \pm 0.1 \times 10^{-21} \text{ molecules}^{-1} \text{ cm}^2 \text{ s}^{-1}$ ). Finally, for the destruction of molecular ozone in the  $\text{H}^+$  experiment,  $k_{-2}$  and  $k_3$  were determined to be  $4.9 \pm 0.3 \times 10^{-8} \text{ s}^{-1}$  and  $5.5 \pm 0.3 \times 10^{-19} \text{ molecules}^{-1} \text{ cm}^2 \text{ s}^{-1}$  respectively, while for the  $\text{He}^+$  experiment these rates were calculated as  $k_{-2} = 1.1 \pm 0.1 \times 10^{-5} \text{ s}^{-1}$  and  $k_3 = 3.0 \pm 0.2 \times 10^{-17} \text{ molecules}^{-1} \text{ cm}^2 \text{ s}^{-1}$ .

The TRIM calculations also calculate the total number of lattice vacancies produced per impinging ion in the oxygen samples. On average, each  $\text{H}^+$  ion was calculated to produce 32 vacancies in the oxygen ice, while a heavier  $\text{He}^+$  ion was calculated to produce 148 vacancies over a shorter stopping range. As each vacancy formed equates to the generation of two oxygen atoms, a total budget of  $5.3 \pm 0.9 \times 10^{17}$  atoms are generated by the  $\text{H}^+$  ions and  $4.4 \pm 0.5 \times 10^{18}$  atoms are produced by  $\text{He}^+$  ions over the respective exposure periods. Furthermore, from the temporal profiles in Fig. 5, the final ozone column density produced in the  $\text{H}^+$  experiment is  $1.5 \pm 0.1 \times 10^{16} \text{ molecules cm}^{-2}$ , corresponding to a total of  $7.7 \pm 0.2 \times 10^{15}$  molecules in the sample. Similarly for the  $\text{He}^+$  irradiation experiments, we measure a total ozone abundance of  $1.4 \pm 0.3 \times 10^{16}$  molecules in the irradiated condensate. For the respective  $\text{H}^+$  and  $\text{He}^+$  experiments, the ozone abundances calculated by intensity of the species FTIR signals are two orders-of-magnitude smaller than the number of oxygen atoms predicted to be generated in the condensate by TRIM vacancy calculations.

### Carbon dioxide ice

**Reaction scheme.** Using a similar method to that used to investigate the kinetic mechanisms unfolding in ion irradiated oxygen ices, we now turn our attention to the reaction

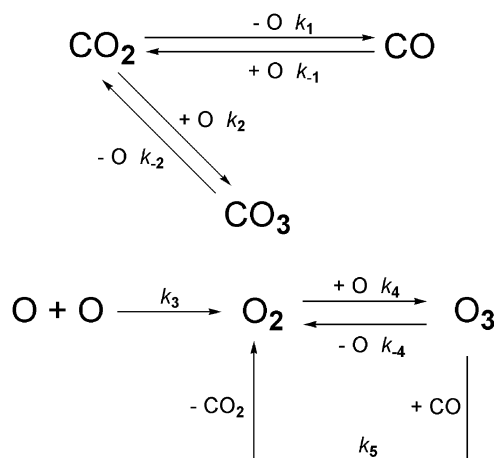


**Fig. 8** Reaction scheme for carbon dioxide ices irradiated with  $\text{H}^+$  and  $\text{He}^+$  ions.

pathways initiated in carbon dioxide condensates by  $\text{H}^+$  and  $\text{He}^+$  irradiation at 12 K. Here, we have developed a reaction scheme with eight pathways (Fig. 8) to untangle the formation routes for our observed irradiation products; carbon monoxide, carbon trioxide, and ozone. The reaction rates were determined for the eight pathways by constructing a set of eight coupled, differential equations to be solved simultaneously.<sup>42–44</sup> The kinetic fits for the carbon dioxide precursor and the carbon monoxide, carbon trioxide, and ozone irradiation products are affixed to the temporal profiles in Fig. 6, optimized to fall within a 5% error margin about the data points. In addition, the abundances of all species were derived directly from the initial column densities of the molecular carbon dioxide precursor,  $[\text{CO}_2]_0$ ; measured to be  $3.8 \pm 0.2 \times 10^{18} \text{ molecules cm}^{-2}$  for the  $\text{H}^+$  experiment and  $4.1 \pm 0.2 \times 10^{18} \text{ molecules cm}^{-2}$  for the  $\text{He}^+$  experiment.

Bombardment with energetic ions induces the decomposition of carbon dioxide *via* homolytic bond cleavage to produce a carbon monoxide molecule and an oxygen molecule in either its ground or first excited electronic state.<sup>19</sup> Carbon dioxide is depleted at a rate  $k_1 \text{ (s}^{-1}\text{)}$ , which can be monitored by the decrease of the carbon dioxide column density and the corresponding increase in the carbon monoxide column density in the temporal profiles for  $\text{H}^+$  and  $\text{He}^+$  exposure (Fig. 6). However, oxygen atoms may recombine with carbon monoxide to regenerate the carbon dioxide molecule at a rate  $k_{-1} \text{ (molecules}^{-1} \text{ cm}^2 \text{ s}^{-1}\text{)}$ . Atomic oxygen generated with sufficient energy to escape the matrix can readily attach to an adjacent ground state carbon dioxide molecule, at rate  $k_2 \text{ (molecules}^{-1} \text{ cm}^2 \text{ s}^{-1}\text{)}$ , to form the cyclic carbon trioxide species. The temporal profiles constructed for carbon trioxide (Fig. 6) indicate that the formation of the species is reversible for both  $\text{H}^+$  and  $\text{He}^+$ , as destruction pathways (rate constant  $k_{-2} \text{ (s}^{-1}\text{)}$ ) are required to fit the carbon trioxide column densities as exposure time continues.

An additional fate for atomic oxygen generated in the carbon dioxide condensate is to recombine with a second oxygen atom to form molecular oxygen, which progresses at rate  $k_3 \text{ (molecules}^{-1} \text{ cm}^2 \text{ s}^{-1}\text{)}$ . Molecular oxygen is not readily identified by spectroscopic analysis and therefore a temporal profile for its abundance in the irradiated ice samples could not be constructed. However, molecular oxygen production was inferred by the formation of molecular ozone, which is more easily identified by FTIR analysis. The temporal profiles for the ozone abundances indicate that pathways are required for the bimolecular production of ozone at rate  $k_4 \text{ (molecules}^{-1} \text{ cm}^2 \text{ s}^{-1}\text{)}$ , and for the radiolytic destruction of the species at rate  $k_{-4} \text{ (s}^{-1}\text{)}$ , both induced in the condensate by continual  $\text{H}^+$  and  $\text{He}^+$  exposure. Finally, an additional destruction mechanism for carbon monoxide was required that did not consume atomic oxygen. The bimolecular reaction between a carbon monoxide molecule and ozone to produce carbon dioxide and molecular oxygen was added to the reaction scheme; this process must occur on an excited state surface.

### Quantification of rate constants and correlation with $S_e/S_n$ .

Adopting the same procedure used to determine energy loss processes by fast ions entering oxygen ice, TRIM simulations

**Table 6** Kinetic data for carbon dioxide irradiation at 12 K

| Pathway  | Reaction scheme  | Rate constants <sup>a</sup>            |  |
|--|--|--|--|
|  |  | H <sup>+</sup>                         | He <sup>+</sup>                        |
| CO <sub>2</sub> destruction/CO formation                                       | CO <sub>2</sub> $\xrightarrow{k_1}$ CO + O                               | $k_1 = 5.2 \pm 0.3 \times 10^{-7}$     | $k_1 = 7.6 \pm 0.4 \times 10^{-5}$     |
| CO destruction/CO <sub>2</sub> formation                                       | CO + O $\xrightarrow{k_{-1}}$ CO <sub>2</sub>                            | $k_{-1} = 1.4 \pm 0.1 \times 10^{-20}$ | $k_{-1} = 1.8 \pm 0.1 \times 10^{-16}$ |
| CO <sub>2</sub> destruction/CO <sub>3</sub> formation                          | CO <sub>2</sub> + O $\xrightarrow{k_2}$ CO <sub>3</sub>                  | $k_2 = 1.4 \pm 0.1 \times 10^{-20}$    | $k_2 = 1.9 \pm 0.1 \times 10^{-20}$    |
| CO <sub>3</sub> destruction/CO <sub>2</sub> formation                          | CO <sub>3</sub> $\xrightarrow{k_{-2}}$ CO <sub>2</sub> + O               | $k_{-2} = 2.4 \pm 0.1 \times 10^{-4}$  | $k_{-2} = 1.3 \pm 0.1 \times 10^{-3}$  |
| O <sub>2</sub> formation   | O + O $\xrightarrow{k_3}$ O <sub>2</sub>                                 | $k_3 = 1.6 \pm 0.1 \times 10^{-14}$    | $k_3 = 7.3 \pm 0.4 \times 10^{-15}$    |
| O <sub>2</sub> destruction/O <sub>3</sub> formation                            | O <sub>2</sub> + O $\xrightarrow{k_4}$ O <sub>3</sub>                    | $k_4 = 6.4 \pm 0.3 \times 10^{-17}$    | $k_4 = 3.0 \pm 0.2 \times 10^{-17}$    |
| O <sub>3</sub> destruction/O <sub>2</sub> formation                            | O <sub>3</sub> $\xrightarrow{k_{-4}}$ O <sub>2</sub> + O                 | $k_{-4} = 5.3 \pm 0.3 \times 10^{-10}$ | $k_{-4} = 1.5 \pm 0.1 \times 10^{-12}$ |
| CO and O <sub>3</sub> destruction/CO <sub>2</sub> and O <sub>2</sub> formation | CO + O <sub>3</sub> $\xrightarrow{k_5}$ CO <sub>2</sub> + O <sub>2</sub> | $k_5 = 1.1 \pm 0.1 \times 10^{-19}$    | $k_5 = 3.4 \pm 0.2 \times 10^{-19}$    |

<sup>a</sup> Unimolecular reaction rate constants  $k_1$ ,  $k_{-2}$ , and  $k_{-4}$  in s<sup>-1</sup> and bimolecular reaction rate constants  $k_{-1}$ ,  $k_2$ ,  $k_3$ ,  $k_4$ , and  $k_5$  in molecules<sup>-1</sup> cm<sup>2</sup> s<sup>-1</sup>.

were performed to calculate the kinetic energy loss of 5 keV H<sup>+</sup> and He<sup>+</sup> ions penetrating the carbon dioxide solids. Compiled in Table 4, the average H<sup>+</sup> ion was determined to transfer a total 37.6 keV μm<sup>-1</sup> to the carbon dioxide ice sample; distributed between electronic interactions,  $S_e = 36.1$  keV μm<sup>-1</sup>, and nuclear collisions,  $S_n = 1.5$  keV μm<sup>-1</sup> ( $S_n/S_e = 0.04$ ). Alternately, for He<sup>+</sup> ions, electronic interactions,  $S_e = 37.5$  keV μm<sup>-1</sup>, and nuclear collisions,  $S_n = 14.6$  keV μm<sup>-1</sup>, sum to a total kinetic energy loss of 52.1 keV μm<sup>-1</sup> ( $S_n/S_e = 0.39$ ) which contributes toward the dissociation of the carbon dioxide molecules.

The rate constants derived for each of the eight reaction pathways are compiled in Table 6. For the initiating reaction, a faster rate was calculated for carbon dioxide dissociation in the He<sup>+</sup> irradiation experiment ( $k_1 = 7.6 \pm 0.4 \times 10^{-5}$  s<sup>-1</sup>) compared to the H<sup>+</sup> experiment ( $k_1 = 5.2 \pm 0.3 \times 10^{-7}$  s<sup>-1</sup>). This is observed to correlate with the total energy transfer from electronic and nuclear collisions for the H<sup>+</sup> ions ( $S = 37.5$  keV μm<sup>-1</sup>) being less than that transferred by the He<sup>+</sup> ions ( $S = 52.0$  keV μm<sup>-1</sup>). This is in addition to the ratio of energy transferred by nuclear interactions *versus* electronic interactions ( $S_n/S_e$ ) being an order of magnitude larger with He<sup>+</sup> than with H<sup>+</sup> particles, resulting in more ‘knock-on’ oxygen atoms *via* He<sup>+</sup> exposure to carbon dioxide. However, this faster rate for atomic oxygen generation in the He<sup>+</sup> experiment is not propagated over the subsequent reaction pathways. For both the H<sup>+</sup> and He<sup>+</sup> experiments, the evolution of carbon trioxide ( $k_2$ ), molecular oxygen ( $k_3$ ), and ozone ( $k_4$ ) are calculated to have production rates of approximately the same order-of-magnitude (Table 6). Therefore, excess reactive oxygen atoms are consumed in the He<sup>+</sup> experiment—by back-reacting with carbon monoxide—at a four order-of-magnitude faster rate ( $k_{-1} = 1.8 \pm 0.1 \times 10^{-16}$  molecules<sup>-1</sup> cm<sup>2</sup> s<sup>-1</sup>) compared to H<sup>+</sup> ( $k_{-1} = 1.4 \pm 0.1 \times 10^{-20}$  molecules<sup>-1</sup> cm<sup>2</sup> s<sup>-1</sup>).

The stopping of a 5 keV H<sup>+</sup> generates an average of 17.2 vacancies in the carbon dioxide ice. In comparison, a 5 keV He<sup>+</sup> ion penetrating the condensate creates 85.4 vacancies before being completely stopped. Excitation of the carbon dioxide molecule *via* inelastic electronic interaction results in the homolytic dissociation of carbon dioxide into an oxygen atom and carbon monoxide molecule. The exposure of the carbon dioxide samples to H<sup>+</sup> ions is calculated to produce a

total budget of  $6.2 \pm 1.6 \times 10^{16}$  oxygen atoms, while He<sup>+</sup> irradiation is calculated to create  $4.8 \pm 1.2 \times 10^{17}$  oxygen atoms, over their respective irradiation periods. As the temporal abundance of molecular oxygen cannot be traced, a complete oxygen budget cannot be resolved. However, by combining the molecular abundances of carbon trioxide and ozone—the formation of each requiring one and three oxygen atoms respectively—we obtain a total of  $2.0 \pm 0.5 \times 10^{15}$  oxygen atoms consumed in the H<sup>+</sup> experiment ( $\Sigma(\text{CO}_3) = 5.3 \pm 0.7 \times 10^{14}$  molecules and  $\Sigma(\text{O}_3) = 4.8 \pm 0.6 \times 10^{14}$  molecules), while the formation of carbon trioxide and ozone induced by He<sup>+</sup> irradiation consumes a total of  $1.2 \pm 0.3 \times 10^{15}$  oxygen atoms ( $\Sigma(\text{CO}_3) = 4.8 \pm 0.6 \times 10^{14}$  molecules and  $\Sigma(\text{O}_3) = 2.5 \pm 0.3 \times 10^{14}$  molecules). In both cases there is significantly less oxygen atoms consumed in the formation of these products than are generated in the vacancy calculations. These oxygen atoms could recombine to molecular oxygen *via* barrier-less atom-atom reactions.

**Comparison of H<sup>+</sup>, He<sup>+</sup>, and e<sup>-</sup> exposure of oxygen and carbon dioxide ices.** The compositional change induced in the molecular ices by the different types of monoenergetic, 5 keV charged species (H<sup>+</sup>, He<sup>+</sup>, e<sup>-</sup>) can now be compared quantitatively. Table 7 compiles the destruction and formation (in molecules eV<sup>-1</sup>) rates for all molecules included in the respective reaction schemes of the irradiating particles as a function of energy. These values are determined for only the first 500 s of exposure, where the exponential kinetic models fitted to the molecular column densities in Fig. 5 and 6 best approximate linear growth and decay profiles. We limit our analysis to this region as our irradiation source produces a much greater flux ( $\Phi(\text{H}^+) = 2.4 \pm 0.9 \times 10^{11}$  particles cm<sup>-2</sup> s<sup>-1</sup>,  $\Phi(\text{He}^+) = 3.6 \pm 1.3 \times 10^{12}$  particles cm<sup>-2</sup> s<sup>-1</sup>,  $\Phi(\text{e}^-) = 2.1 \pm 0.6 \times 10^{11}$  particles cm<sup>-2</sup> s<sup>-1</sup>) than experienced in Solar System environments ( $\Phi(\text{total}) = \sim 10$  particles cm<sup>-2</sup> s<sup>-1</sup>).

Previous experiments<sup>25</sup> performed on oxygen ice have shown that 5 keV electron irradiation degrades oxygen ice ( $-7.2 \pm 2.0 \times 10^{-3}$  molecules eV<sup>-1</sup>) more efficiently than the 5 keV H<sup>+</sup> ( $-2.2 \pm 0.7 \times 10^{-3}$  molecules eV<sup>-1</sup>) and He<sup>+</sup> ions ( $-1.7 \pm 0.5 \times 10^{-3}$  molecules eV<sup>-1</sup>) used in the present study. It follows that electron irradiation induced an order-of-magnitude

**Table 7** Destruction and formation yields induced in oxygen and carbon dioxide ices by particle irradiation

| Molecule           | H <sup>+</sup> /molecules eV <sup>-1</sup> | He <sup>+</sup> /molecules eV <sup>-1</sup> | e <sup>-</sup> /molecules eV <sup>-1</sup> |
|--------------------|--|---|--|
| Oxygen ice         |  |   |  |
| O <sub>2</sub>     | $-2.2 \pm 0.7 \times 10^{-3}$              | $-1.7 \pm 0.5 \times 10^{-3}$               | $-7.2 \pm 2 \times 10^{-3a}$               |
| O <sub>3</sub>     | $1.5 \pm 0.5 \times 10^{-3}$               | $1.3 \pm 0.4 \times 10^{-3}$                | $16 \pm 4 \times 10^{-3a}$                 |
| Carbon dioxide ice |  |   |  |
| CO <sub>2</sub>    | $-1.7 \pm 0.7 \times 10^{-3}$              | $-2.2 \pm 1.0 \times 10^{-3}$               | $-11 \pm 3 \times 10^{-3b}$                |
| CO                 | $1.5 \pm 0.6 \times 10^{-3}$               | $1.8 \pm 0.8 \times 10^{-3}$                | $16 \pm 4 \times 10^{-3b}$                 |
| CO <sub>3</sub>    | $2.2 \pm 0.9 \times 10^{-4}$               | $1.6 \pm 0.7 \times 10^{-4}$                | $17 \pm 5 \times 10^{-4b}$                 |
| O <sub>2</sub>     | $1.8 \pm 0.8 \times 10^{-4}$               | $6.6 \pm 2.9 \times 10^{-4}$                | $25 \pm 7 \times 10^{-4a}$                 |
| O <sub>3</sub>     | $40 \pm 17 \times 10^{-5}$                 | $9.6 \pm 4.2 \times 10^{-5}$                | $200 \pm 60 \times 10^{-5a}$               |

<sup>a</sup> Bennett and Kaiser (2005). <sup>b</sup> Bennett *et al.* (2004).

greater ozone yield ( $16 \pm 4 \times 10^{-3}$  molecules eV<sup>-1</sup>) than fast H<sup>+</sup> ( $1.5 \pm 0.5 \times 10^{-3}$  molecules eV<sup>-1</sup>) and He<sup>+</sup> ions ( $1.3 \pm 0.4 \times 10^{-3}$  molecules eV<sup>-1</sup>). The higher ozone yield produced by 5 keV electrons can be attributed to these particles dissipating their kinetic energy to the system exclusively *via* inelastic electronic interactions ( $S_e$ ) with the target molecules. These interactions generate a cascade of secondary electrons ejected from ionized target molecules, with some possessing energies within the  $\sim 1$ –10 eV range. Such energies are of sufficient order to induce homolytic bond cleavage within the surrounding molecules and create reactive radical species in the ice environment. This is opposed to the more massive 5 keV H<sup>+</sup> ( $S_e/(S_e + S_n) = 0.95$ ) and He<sup>+</sup> particles ( $S_e/(S_e + S_n) = 0.69$ ), which only transmit a proportion of their kinetic energy to electronic interactions ( $S_e$ ) and hence produce a lower number density of secondary electrons. The balance of the H<sup>+</sup> and He<sup>+</sup> kinetic energy is dissipated to nuclear interactions, ( $S_n$ ), which become increasingly important as the particles slow in the solid—forming vacancies through ion–target collisions. However, as ozone formation appears correlated to the electronic stopping potential of the incident irradiation, electron irradiation, with a  $S_e/(S_e + S_n)$  of unity, leads to a considerably higher number of oxygen molecule dissociations within the sample. On the other hand, the implanted H<sup>+</sup> and He<sup>+</sup> are calculated to generate less secondary electrons *via* inelastic electronic collisions, resulting in a lower number of target molecule dissociating to form atomic oxygen and, hence, a subsequent ozone yield.

The relationship between the destruction and formation values calculated for carbon dioxide ices irradiated with H<sup>+</sup>, He<sup>+</sup>, and electrons are similar to those observed in the irradiated oxygen ices. The destruction of carbon dioxide ( $-11 \pm 3 \times 10^{-3}$  molecules eV<sup>-1</sup>) induced by 5 keV electrons and the subsequent formation of carbon monoxide ( $16 \pm 4 \times 10^{-3}$  molecules eV<sup>-1</sup>), carbon trioxide ( $17 \pm 5 \times 10^{-4}$  molecules eV<sup>-1</sup>), and molecular oxygen ( $25 \pm 7 \times 10^{-4}$  molecules eV<sup>-1</sup>) are an order-of-magnitude greater than the values produced by the interaction of fast H<sup>+</sup> and He<sup>+</sup> ions (Table 7). In addition, the values obtained for H<sup>+</sup> and He<sup>+</sup> irradiation are within each other's error limits, except for the production of molecular oxygen by He<sup>+</sup> ( $6.6 \pm 2.9 \times 10^{-4}$  molecules eV<sup>-1</sup>) which is greater than the value obtained by H<sup>+</sup> ( $1.8 \pm 0.8 \times 10^{-4}$  molecules eV<sup>-1</sup>). However, the greatest disparity between the irradiated carbon dioxide product values is for ozone formation, where the yield returned for He<sup>+</sup> ions ( $9.6 \pm 4.2 \times 10^{-5}$  molecules eV<sup>-1</sup>) is a factor of four

less than H<sup>+</sup> irradiation ( $40 \pm 17 \times 10^{-5}$  molecules eV<sup>-1</sup>) and a further factor or twenty less than the ozone generated with electrons ( $200 \pm 60 \times 10^{-5}$  molecules eV<sup>-1</sup>). As discussed for the oxygen ice above, the dissociation of carbon dioxide molecules into reactive intermediates is thought to be governed by the number density of secondary electrons produced in the condensate. It is suggested that for this reason, 5 keV electrons dissipating energy exclusively *via* the electronic stopping potential are more efficient in generating new molecular species in the carbon dioxide ice.

Note that the number of secondary electrons generated in the oxygen and carbon dioxide condensates differs with the irradiating particle. In the case of a 5 keV electron impinging a surface (LET  $\approx 5$  keV  $\mu\text{m}^{-1}$ ) we may expect only a few secondary electrons to be produced per micron, with average energies in the bond-rupturing range of 10–100 eV (however, with a possible maxima of 2500 eV). In contrast, 5 keV H<sup>+</sup> and He<sup>+</sup> ions, with their considerably higher LET values (Table 4), could eject 10–100's of secondary electrons before they come to rest in the solid. However, the average kinetic energy of ion-induced secondary electrons in this case (keV range) is too high to efficiently promote dissociation of the target molecules.

## Conclusions

Processing of oxygen-bearing ices by energetic ion irradiation is of particular importance in the context of apolar ices (ices containing carbon monoxide, carbon dioxide, and molecular oxygen and nitrogen) which accumulate on the outer layers of interstellar dust particles.<sup>46</sup> Distributed through the confines of dense molecular clouds, grain particles act as substrates for polar (water dominant) and apolar ices which accumulate as gas-phase species (with the exception of H, H<sub>2</sub>, and He) accrete on their surfaces at ultralow temperatures (as low as 10 K).<sup>47</sup> Harbored within interstellar media, these icy mantles are exposed to GCR particles. Such particles are of sufficient energy to initiate chemical processes in the material upon impact. As shown in the present study, fast H<sup>+</sup> and He<sup>+</sup> ions undergo electronic and nuclear energy loss *via* collisions with the molecular composition of oxygen and carbon dioxide ices. The replication of these impacts in the laboratory indicates that a number of product species, such as ozone and cyclic carbon trioxide can be efficiently generated on these surfaces from the formation of suprathreshold atomic

oxygen and its recombination with the precursor oxygen and carbon dioxide molecules.

Although ozone has yet to be detected as a component of interstellar ices by remote IR spectroscopy, as its bands are shrouded by dominant absorption features from the silicate substrate, it has been presumed that the species is an abundant component of these materials. Ozone is commonly incorporated into the chemical models associated with the formation of water molecules in polar ices through hydrogen implantation.<sup>48</sup> Extending on this development, the present study shows that the presence of ozone is of similar importance in apolar ices. As the abundance of ozone ( $T_{\text{sub}} = 60$  K) increases at the expense of carbon dioxide ( $T_{\text{sub}} = 90$  K), the annealing of the grain particles as they intersperse through the interstellar medium, for example from quiescent cloud environments to warm protostellar regions, would promote the sublimation of ozone. This would be in preference to the out-gassing of carbon dioxide with its higher sublimation temperature from the apolar ice mantle surfaces. It can therefore be reasoned that such processes may contribute to the differences in molecular composition observed for interstellar grains from diverse cloud environments.<sup>49</sup>

Debate continues regarding the identification of cyclic carbon trioxide in interstellar ices as the strongest IR absorption band associated with the species, the  $\nu_1(\text{CO}_3)$  carboxyl group stretch at  $\sim 2045$   $\text{cm}^{-1}$ , overlaps with the C=O band of carbonyl sulfide (OCS) molecule which is also proposed to be present in the grains in low abundances. The laboratory simulations conducted in the present study confirms that carbon trioxide is produced in significant quantities *via* the irradiation of low temperature carbon dioxide by energetic  $\text{H}^+$  and  $\text{He}^+$  ions. As these experiments were conducted at temperatures representative of interstellar media (12 K), it is likely carbon trioxide remains stable in the grain composition once formed, as the species does not decompose until reaching temperatures of  $\sim 90$  K.<sup>20</sup> For this reason carbon trioxide can act to conserve the abundance of oxygen in the apolar ice composition, as opposed to the generation of volatile molecular oxygen and ozone.

In addition to interstellar grains, molecular oxygen and carbon dioxide have been detected on numerous Galilean and Saturnian satellites. Here, harbored within predominantly water ice matrices, they are exposed to collisions with charged particles entrapped in planetary magnetospheres and particles from solar and GCR irradiation, particularly fast  $\text{H}^+$  and  $\text{He}^+$  ions. As shown in the experiments performed in this investigation, radiolysis induced processes are expected to be initiated in these low temperature environments, where chemical pathways dictated by atomic oxygen generation and subsequent recombination with the molecular oxygen and carbon dioxide precursors are likely to result in the formation of ozone and carbon trioxide respectively. However, these processes are far from isolated. As Solar System ices also contain a rich inventory of hydrogen and nitrogen-bearing molecules, the irradiation induced production of compounds such as ozone and carbon trioxide can be considered as intermediate steps *en route* to higher order and potentially biologically important species.

## Acknowledgements

CPE and RIK thank the Air Force Office of Scientific Research (A9550-09-1-0177) for support. CJB thanks the National Aeronautics Space Administration (NASA Astrobiology Institute under Cooperative Agreement no. NNA09DA77A issued through the Office of Space Science) for funding.

## References

- 1 A. P. Showman and R. Malhotra, *Science*, 1999, **286**, 77–84.
- 2 J. F. Cooper, R. E. Johnson, B. H. Mauk, H. B. Garrett and N. Gehrels, *Icarus*, 2001, **149**, 133–159.
- 3 R. H. Brown, R. N. Clark, B. J. Buratti, D. P. Cruikshank, J. W. Barnes, R. M. E. Mastrapa, J. Bauer, S. Newman, T. Momary, K. H. Baines, G. Bellucci, F. Capaccioni, P. Cerroni, M. Combes, A. Coradini, P. Drossart, V. Formisano, R. Jaumann, Y. Langevin, D. L. Matson, T. B. McCord, R. M. Nelson, P. D. Nicholson, B. Sicardy and C. Sotin, *Science*, 2006, **311**, 1425–1428.
- 4 D. P. Cruikshank, A. W. Meyer, R. H. Brown, R. N. Clark, R. Jaumann, K. Stephan, C. A. Hibbitts, S. A. Sandford, R. M. E. Mastrapa, G. Filacchione, C. M. Dalle Ore, P. D. Nicholson, B. J. Buratti, T. B. McCord, R. M. Nelson, J. B. Dalton, K. H. Baines and D. L. Matson, *Icarus*, 2010, **206**, 561–572.
- 5 J. Crovisier, K. Leech, D. Bockelee-Morvan, T. Y. Brooke, M. S. Hanner, B. Altieri, H. U. Keller and E. Lellouch, *Science*, 1997, **275**, 1904–1907.
- 6 C. Waelkens, K. Malfait and L. B. F. M. Waters, *Earth, Moon, and Planets*, 1999, **79**, 265–274.
- 7 E. L. Gibb, D. C. B. Whittet, A. C. A. Boogert and A. G. G. M. Tielens, *Astrophys. J. Suppl.*, 2004, **151**, 35–73.
- 8 A. Nummelin, D. C. B. Whittet, E. L. Gibb, P. A. Gerakines and J. E. Chiar, *Astrophys. J.*, 2001, **558**, 185–193.
- 9 P. Ehrenfreund and E. F. Van Dishoeck, *Adv. Space Res.*, 1998, **21**, 15–20.
- 10 J. R. Spencer, W. M. Calvin and M. J. Person, *J. Geophys. Res.*, 1995, **100**, 19049–19056.
- 11 J. R. Spencer and W. M. Calvin, *Astron. J.*, 2002, **124**, 3400–3403.
- 12 P. D. Cooper, M. H. Moore and R. L. Hudson, *Icarus*, 2008, **194**, 379–388.
- 13 W. Zheng, D. Jewitt and R. I. Kaiser, *Astrophys. J.*, 2006, **639**, 534–548.
- 14 W. Zheng, D. Jewitt and R. I. Kaiser, *Astrophys. J.*, 2006, **648**, 753–761.
- 15 J. F. Kasting and D. Catling, *Annu. Rev. Astron. Astrophys.*, 2003, **41**, 429–463.
- 16 K. S. Noll, R. E. Johnson, A. L. Lane, D. L. Domingue and H. A. Weaver, *Science*, 1996, **273**, 341–343.
- 17 K. S. Noll, T. L. Roush, D. P. Cruikshank, R. E. Johnson and Y. J. Pendleton, *Nature*, 1997, **388**, 45–47.
- 18 R. E. Johnson, *Energetic Charged-Particle Interactions with Atmospheres and Surfaces*, Springer-Verlag, Berlin, 1990.
- 19 C. J. Bennett, C. Jamieson, A. M. Mebel and R. I. Kaiser, *Phys. Chem. Chem. Phys.*, 2004, **6**, 735–746.
- 20 R. I. Kaiser and A. M. Mebel, *Chem. Phys. Lett.*, 2008, **465**, 1–9.
- 21 C. J. Bennett, C. S. Jamieson and R. I. Kaiser, *Phys. Chem. Chem. Phys.*, 2010, **12**, 4032–4050.
- 22 C. S. Jamieson, A. M. Mebel and R. I. Kaiser, *Chem. Phys. Lett.*, 2007, **440**, 105–109.
- 23 C. S. Jamieson, A. M. Mebel and R. I. Kaiser, *Chem. Phys. Lett.*, 2007, **443**, 49–54.
- 24 C. S. Jamieson, A. M. Mebel and R. I. Kaiser, *Chem. Phys. Lett.*, 2007, **450**, 312–317.
- 25 C. J. Bennett and R. I. Kaiser, *Astrophys. J.*, 2005, **635**, 1362–1369.
- 26 R. A. Baragiola, C. L. Atteberry, D. A. Bahr and M. M. Jakas, *Nucl. Instrum. Methods Phys. Res., Sect. B*, 1999, **157**, 233–238.
- 27 M. Fama, D. A. Bahr, B. D. Teolis and R. A. Baragiola, *Nucl. Instrum. Methods Phys. Res., Sect. B*, 2002, **193**, 775–780.
- 28 M. Garozzo, D. Fulvio, O. Gomis, M. E. Palumbo and G. Strazzulla, *Planet. Space Sci.*, 2008, **56**, 1300–1308.

- 
- 29 E. S. Duarte, P. Boduch, H. Rothard, T. Been, E. Dartois, L. S. Farenzena and E. F. da Silveira, *Astron. Astrophys.*, 2009, **502**, 599–603.
- 30 R. I. Kaiser, P. Jansen, K. Petersen and K. Roessler, *Rev. Sci. Instrum.*, 1995, **66**, 5226–5231.
- 31 W. Zheng, D. Jewitt and R. I. Kaiser, *J. Phys. Chem. A*, 2009, **113**, 11174–11181.
- 32 Y. A. Freiman and H. J. Jodl, *Phys. Rep.*, 2004, **401**, 1–228.
- 33 *NATO Advanced Science Institutes Series, C: Mathematical and Physical Sciences*, in *Ices in the Solar System*, ed. J. Klinger, D. Benest, A. Dollfus and R. Smoluchowski, D. Riedel, Dordrecht, 1985, vol. 156, [Proceedings of a Workshop Held in Nice, Fr., January 16–19, 1984].
- 34 J. F. Ziegler, M. D. Ziegler and J. P. Biersack, SRIM-2008.04 edn., Annapolis, 2008.
- 35 L. Brewer and J. L. F. Wang, *J. Chem. Phys.*, 1972, **56**, 759–762.
- 36 S. A. Sandford and L. J. Allamandola, *Astrophys. J.*, 1990, **355**, 357–372.
- 37 K. A. Newson, S. M. Luc, S. D. Price and N. J. Mason, *Int. J. Mass Spectrom. Ion Processes*, 1995, **148**, 203–213.
- 38 B. Vandenbussche, P. Ehrenfreund, A. C. A. Boogert, E. F. Van Dishoeck, W. A. Schutte, P. A. Gerakines, J. Chiar, A. G. G. M. Tielens, J. Keane, D. C. B. Whittet, M. Breittfellner and M. Burgdorf, *Astron. Astrophys.*, 1999, **346**, L57–L60.
- 39 S. M. Adler-Golden, S. R. Langhoff, C. W. Bauschlicher Jr. and G. D. Carney, *J. Chem. Phys.*, 1985, **83**, 255–264.
- 40 P. A. Gerakines, W. A. Schutte, J. M. Greenberg and E. F. Van Dishoeck, *Astron. Astrophys.*, 1995, **296**, 810–818.
- 41 G. J. Jiang, W. B. Person and K. G. Brown, *J. Chem. Phys.*, 1975, **62**, 1201–1211.
- 42 M. Frenklach, A. Packard and R. Feelet, in *Modeling of Chemical Reactions*, ed. R. W. Carr, Elsevier, Amsterdam, 2007, vol. 42, p. 243.
- 43 M. Frenklach, H. Wang and M. J. Rabinowitz, *Prog. Energy Combust. Sci.*, 1992, **18**, 47–73.
- 44 M. Frenklach, *Combust. Flame*, 1984, **58**, 69–72.
- 45 P. C. Cosby, *J. Chem. Phys.*, 1993, **98**, 9560–9569.
- 46 P. Ehrenfreund, A. Boogert, P. Gerakines and A. Tielens, *Faraday Discuss.*, 1998, **109**, 463–474.
- 47 V. Mennella, M. E. Palumbo and G. A. Baratta, *Astrophys. J.*, 2004, **615**, 1073–1080.
- 48 H. Mokrane, H. Chaabouni, M. Accolla, E. Congiu, F. Dulieu, M. Chehrouri and J. L. Lemaire, *Astrophys. J.*, 2009, **705**, L195–L198.
- 49 J. Elsila, L. J. Allamandola and S. A. Sandford, *Astrophys. J.*, 1997, **479**, 818–838.